ISPRS Journal of Photogrammetry and Remote Sensing 183 (2022) 389–402

Contents lists available at ScienceDirect

ISPRS Journal of Photogrammetry and Remote Sensing

journal homepage: www.elsevier.com/locate/isprsjprs

An improved methodology for quantifying pixel-scale entrance pupil irradiance of a Moon-based Earth radiation observatory

Wentao Duan [a], Shuanggen Jin [a,b,*]

[a] School of Remote Sensing and Geomatics Engineering, Nanjing University of Information Science and Technology, Nanjing 210044, China
[b] Shanghai Astronomical Observatory, Chinese Academy of Sciences (CAS), Shanghai 200030, China

ARTICLE INFO

Keywords:
Earth radiation budget
Pixel-scale entrance pupil irradiance
Moon-based Earth Radiation Observatory

ABSTRACT

The establishment of a Moon-based Earth Radiation Observatory (MERO) is expected to improve current Earth radiation budget observations. In terms of the MERO instrument design, the pixel-scale entrance pupil irradiance (EPI), which acts as the true input radiation to the MERO detector unit, is essential to judge the detector optimization and systematic parameter adjustment. The primary motivation of this study is to improve the pixel-scale EPI quantification quality by proposing a modified methodology. Evaluations indicated that the new pixel ground field of view (GFOV) positioning method would bring accuracy improvements of 7.79% and 3.84% for pixel-scale shortwave (SW) EPI and longwave (LW) EPI quantifications respectively; while the accuracy enhancements result from the newly proposed Earth top of atmosphere (TOA) radiant anisotropy method in this study are about 20.67% and 12.15% for the pixel-scale SW EPI and LW EPI estimations respectively. Following this modified methodology, an 18.6-year pixel-scale EPI variability prediction was accomplished to facilitate the MERO instrument design coping with change in future decades. This prediction fully considers the influences from the MERO-Earth geometry evolution, Earth TOA radiant anisotropic factor temporal change, the Earth TOA flux temporal variation and MERO location change. Results showed that the SW EPI would vary from approximately 3.32×10^{-6} to 2.16×10^{-4} W/m^2 over the future 18.6-year period (March 2019 to November 2037); while the LW EPI would change between 4.43×10^{-6} and 4.91×10^{-4} W/m^2.

1. Introduction

Global climate change is substantially affected by the budget of the incoming and outgoing energy of the Earth system (Brown and Caldeira 2017). The incoming energy consists mainly of solar radiation, whereas the outgoing energy is predominantly comprised of two parts, namely, the reflected solar shortwave (SW) radiation and the emitted longwave (LW) radiation (Kopp and Lean 2011; Wong et al. 2018). Both the reflected SW solar radiation and emitted LW radiation vary over a small temporal scale and a global spatial scale. This feature enables the space platforms to act as the main Earth Radiation Budget (ERB) monitoring systems (Trenberth et al. 2009; Wielicki et al. 2002). Since the 1970 s, several satellite-based ERB observatories have been launched, including The Earth Radiation Budget Experiment (ERBE) (Barkstrom et al. 1989; Forster and Gregory 2006; Zhou et al. 2016), the Cloud and the Earth's Radiant Energy System (CERES) (Trepte et al. 2019), the Geostationary Earth Radiation Budget (GERB) onboard the Meteosat Second Generation satellites (Dewitte et al. 2008; Harries et al. 2005) and the National Institute of Standards and Technology Advanced Radiometer (NISTAR) onboard the Deep Space Climate Observatory (DSCOVR) spacecraft (Marshak et al. 2018; Su et al. 2020).

Though current satellite observations have indeed enhanced our understanding of the ERB and its influence on climate change (Guo et al. 2016), they still have several limitations, which we think could be complemented by a Moon-based Earth Radiation Observatory (MERO). Below illustrates the detailed advantages of a MERO compared to current satellite-based ERB systems. (1) Generally, a satellite-based ERB mission needs a constellation to accomplish the global ERB observation, however, fusion of data from various satellite sensors would suffer from the viewing geometry difference among multi-satellites, which hampers the data consistency. In contrast, the data inconsistency resulting from the viewing geometry difference is much lesser for multiple MERO systems (Guo et al. 2019). Because the Earth–Moon distance (380,000 km on average) is about 100 times greater than the diameter of the Moon

* Corresponding author at: School of Remote Sensing and Geomatics Engineering, Nanjing University of Information Science and Technology, Nanjing 210044, China.
E-mail addresses: eilen4011@nuist.edu.cn (W. Duan), sgjin@nuist.edu.cn (S. Jin).

https://doi.org/10.1016/j.isprsjprs.2021.11.019
Received 26 August 2021; Received in revised form 18 November 2021; Accepted 24 November 2021
Available online 4 December 2021

(3476 km), the distance between any site on the near-side of Moon and the Earth's center only differs by less than 5%, and the Earth viewing angle (the viewing zenith angle or viewing azimuth angle) change is less than 2% (Duan et al. 2018). This indicates that differently located MERO sensors launched at various periods would share a highly similar geometry towards Earth, which facilitates the production of long-term ERB records with good consistency by merging data from different MERO missions. (2) Current and previous low-Earth-orbit (LEO) ERB systems could not capture the Earth's system's inherently small-time-scale outgoing SW and LW radiations with an acceptable accuracy partially due to the limited temporal coverage (Smith et al. 2015). In comparison, a MERO has the potential to provide far higher temporal coverage than the LEO ERB systems. Since the MERO sensor field of view (FOV) covers the whole Earth disk, a certain location on the Earth can be continuously observed by a MERO for 12 h per day on average. If the sampling frequency is assumed to be every 15 min (the GERB sampling frequency), a MERO would obtain 48 temporal samples in a diurnal cycle, which is approximately 24 times greater than that of a low-orbit ERB instrument. These samples could evidently improve the assessment of the small-time scale outgoing SW and LW radiations of the Earth, and efficiently enhance the quality of the ERB diurnal cycle data produced by the ERB fitting method (Smith et al. 2015). (3) A MERO sensor could derive the instantaneous TOA flux map of the whole Earth disk at a certain spatial resolution (spatial resolution depends on the number of detector units). Such maps are able to substantially reduce the uncertainty brought by the non-simultaneous sampling of the spatial variability of the TOA flux, which is one of the main error sources of the LEO ERB systems. Besides, almost all locations within a certain region on Earth (such as 3° latitude × 3° longitude) could be simultaneously sampled by a MERO for a long time (e.g., 12 h per day), which helps to reveal the small-temporal-scale regional energy exchange precisely. In contrast, the NISTAR onboard DSCOVR is a single-detector sensor, which just produce one incident flux value that is contributed by the whole Earth disk at a temporal sampling; however, this single incident flux is difficult to be reliably converted to the TOA flux map of the whole Earth disk in regional spatial resolution. (4) A MERO could partially complement the insufficiencies in current satellite-based ERB observations of polar regions. Due to the limited temporal samples in a diurnal cycle, the LEO ERB system could not provide small-temporal-scale ERB observations in satisfied accuracy, which are essential for understanding the energy balance in Antarctic/Arctic region during transition periods (e.g., the melting and frozen periods). Owing to the altitude restriction, current geostationary-Earth-orbit (GEO) ERB system could just provide observations with very oblique viewing geometry for polar regions, which bring coarse spatial resolution and evident measurement uncertainty (Hall et al. 2019; Harries et al. 2005). In comparison, a MERO has the ability to continuously observe a Arctic or Antarctic location for>12 h per day during half of a lunar orbital period with an acceptable viewing geometry (Duan et al. 2018). This enables a MERO to result in ERB data with much higher temporal resolution for polar regions, facilitating reliably revealing small time scale variability of TOA outgoing SW and LW radiations over Arctic and Antarctic regions.

The realization of a MERO has become more likely recently as the new project of the China's Chang-E lunar exploration began. At current pre-implementation stage, instrument design is the key task (Luther et al. 1986; Smith et al. 2014). The basic scientific objective of the MERO mission is to measure the Earth reflected outgoing shortwave flux at TOA in the 0.2–4 μm wavelength, and the outgoing longwave flux at TOA in the wavelength of 4–100 μm range. In our previous study (Duan et al. 2019), a wide-field-of-view single-detector radiometer is proposed for the MERO mission, such an instrument just has one detector to simultaneously observe half of the globe; at each temporal sampling, there will be just one measured incident flux value, which is the integration of the radiances from the whole Earth disk. However, since there exists a remarkable spatial variability in the TOA SW and LW fluxes of the whole Earth disk, this single measured incident flux value could not be reliably converted to an instantaneously Earth TOA flux map of the observed whole-Earth disk in an acceptable spatial resolution. Notably, producing such a map is one of the core scientific objectives of the MERO mission, which is illustrated above. To overcome this drawback, we have upgraded the MERO sensor concept to a multi-pixel (detector unit) non-scanner imaging spectroradiometer with a focal plane array (FPA, which is the aggregation of multiple detector units) (Rogalski 2012). The multi-pixel MERO instrument works like a camera: at each temporal sampling, the whole FPA would simultaneously "photograph" the TOA outgoing SW and LW radiations of the entire Earth disk, while one detector unit (pixel) (the solid green rectangle in the upper left of Fig. 1) in the FPA would just instantaneously "photograph" the outgoing SW and LW radiations of a certain TOA region (the hollow green rectangle in the bottom right of Fig. 1, this certain TOA region is defined as the ground field of view (GFOV) corresponding to the pixel). One pixel in the FPA is an independent system, it transforms the received incident flux (entrance pupil irradiance, abbreviated as EPI) from the pixel GFOV to the electrical signal, which is then processed to the digital number by the readout circuit linked to the detector unit; afterwards, this digital number is converted to the measured EPI by the radiometric calibration function, such measured EPI would then be transformed to the measured incident radiance using the MERO pixel (detector unit) observing geometry. Then, this incident radiance would be converted to the measured TOA flux of the pixel GFOV using the Earth TOA radiant anisotropic factor. Finally, when all the pixels finish their work flow, the instantaneously whole-Earth-disk TOA flux map in regional spatial resolution could be derived.

As indicated by the multi-pixel MERO instrument work flow described above, the entrance pupil irradiance (EPI) of one detector unit (pixel) is the actual incident flux into the pixel, which is the true value of the MERO level-0 measurement data. For MERO instrument design, the pixel-scale EPI could act as a "referee" to provide strong constrains. For example, the optimal choice could be reliably made among various detector options by testing their signal qualities and operating stabilities in response to the EPI (Haran et al. 2019; Rogalski 2010, pp. 645-676). The pixel-scale EPI could also be utilized to judge the certain parameter adjustment for a MERO FPA, such as the responsivity and detectivity (Rogalski 2012). Besides, the EPI quantification accuracy would affect the MERO data quality. One core step of MERO data producing is to converse the digital number (DN) value to the measure EPI using the radiation calibration function (RCF); RCF is the relationship between the "true EPI" and the DN value. However, since the degradation of the sensor and the variance of the true EPI, the RCF needs to be frequently corrected. Accordingly, a reliable source of this "true" EPI in on-orbit calibration is important. In fact, one vital source for this "true EPI" is the pixel-scale EPI quantification utilizing the in-situ measurement of the Earth TOA flux (such TOA flux can be derived by the in-situ measurement of ground radiation and radiative transfer calculations) (Czapla-Myers et al. 2015; Thorne et al. 1997). Other"true EPI" sources include the inner calibration module (ICM) and inter calibration process supported by other sensors. However, the ICM is subject to the degradation, and the inter-calibration is substantially affected by the accuracy of the compared sensor. Furthermore, the pixel-scale EPI quantification plays an important role in determining the specification of the ICM of the MERO system (ICM is dedicated to provide the "true" EPI to correct the RCF). The pixel-scale EPI can also be used to evaluate the spatial and temporal resolution options for the MERO instrument design. As indicated above, the pixel-scale EPI could be converted to the instantaneously regional whole-Earth disk TOA flux map. Comparisons of the qualities of these MERO-measured flux maps produced by all spatial and temporal resolution options can concretely select the optimal sensor resolution scheme.

Altogether, the pixel-scale EPI quantification is vital for the pre-launch instrument design and after-launch data production of the MERO system. However, current effort paid on this topic is still substantially scarce through we have accomplished two MERO EPI studies.

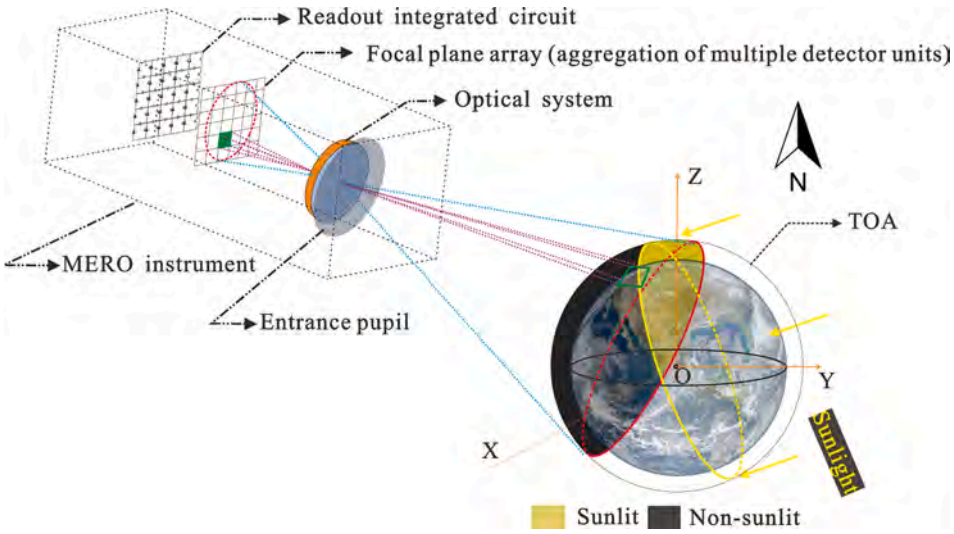

Fig. 1. A diagram to show how a multi-pixel MERO sensor works. In general, this sensor operates like a camera. At a temporal sampling, the focal plane array (abbreviated as FPA, which is the aggregation of multiple detector units) would simultaneously "photograph" the TOA outgoing SW and LW radiations of the whole Earth disk, while one detector unit (pixel) (the solid green rectangle on the upper left) in the FPA would just instantaneously "photograph" the outgoing SW and LW radiations of a certain TOA region (the hollow green rectangle on the bottom right, this certain TOA region is defined as the ground field of view (GFOV) corresponding to the pixel). (For interpretation of the references to colour in this figure legend, the reader is referred to the web version of this article.)

In general, the pixel-scale EPI quantification involves three major parts: (1) the pixel GFOV positioning method, which finds the exact position of the pixel GFOV and determines the MERO-Earth geometry; (2) the "absolute" Earth TOA flux of known accuracy; and (3) the Earth TOA radiant anisotropy method, which determines the directional radiance from the TOA flux. Our first EPI study is made for a wide-field-of-view single-detector (pixel) MERO sensor (Duan et al. 2019), the pixel GFOV is the whole Earth disk; therefore, its GFOV positioning method could not be used for the multi-pixel MERO instrument. Besides, this first stage study didn't consider the TOA SW radiant anisotropy and adopted an oversimplified LW radiant anisotropy, which would introduce remarkable uncertainty to the EPI computation. Hence, we made several methodological improvements in our second stage EPI study (Duan and Jin 2019); we proposed a preliminary pixel GFOV positioning approach and adopted a new TOA SW anisotropy method which partially considered the effect from the viewing geometry variation. However, such a preliminary approach would result in an incorrect position for the pixel GFOV and the TOA radiant anisotropy method is still over-simplified without adequate consideration of the remarkable effects from related factors; all these would introduce obvious uncertainties.

To overcome these defects, we proposed an all-new pixel GFOV positioning method based on the projection in this study, which could make the method determined pixel GFOV keep well consistent with the actual one to evidently reduce the uncertainty induced by the mismatch. Furthermore, this study adopted a much more realistic TOA SW and LW radiant anisotropy methods with full consideration of the influences from related factors, such as surface type, certain cloud and meteorological parameters and viewing geometry (details about these methodologic improvements made in this study and the brought accuracy enhancement are exhibited in section 3). Following these methodology enhancements, we made a long-term (18.6-year) pixel-scale EPI variability prediction in this study to facilitate the MERO instrument design coping with changes in the future decades. This paper is organized as follows. Section 2 mainly describes the EPI quantification methodology. Section 3 is dedicated to the description of the methodologic improvements made in this study compared to our previously published EPI works. Section 4 describes the results of the long-term (18.6-year) EPI variability prediction. Sections 5 and 6 provide the discussion and main conclusions, respectively.

2. Methodology

2.1. Sensor field of view (FOV) and FPA structure

The pixel-scale EPI is closely related to the sensor FOV and FPA structure (pixel distribution). The minimum MERO sensor FOV that is required to covers the full Earth disk would temporal vary due to the time-dependent variability of the Moon-Earth distance induced by the elliptical shape of the Moon's orbit. To avoid the frequent adjustment of the FOV that would shorten the longevity of the instrument, we concluded a unchanged sensor FOV of approximately 2.07° that could always cover the full Earth disk over the future 18.6 years (April 2017 to November 2035) in our previous study (Duan et al. 2018). However, this unchanged sensor FOV would lead to a slight over-coverage in most cases (Fig. 2 (a)), that is, the imaging area of the FPA (red circle in Fig. 2 (b)) would be larger than the actual area of the observed whole Earth disk (half-transparent whole Earth disk image in Fig. 2 (b)).

The FPA (aggregation of numbers of detector units) structure is shown in Fig. 2 (b), in this study, we adopted a spatial resolution of 800 km (at the Earth equator) for the MERO sensor due to our limited computation resources. To complement this defect, we have set the spatial resolution as a global variable in the computer code of this study, therefore, the pixel-scale EPI quantification for MERO sensor with higher spatial resolution can also be successfully conducted based on the codes of this research when adequate computation capacity is obtained in the future. We have distributed the pixels (detector units) according to the circular imaging border (red circle in Fig. 2 (b)), and coded each pixel in number to distinguish them. Such FPA structure (pixel distribution) could avoid the waste of the corner pixels compared to the rectangle FPA layout.

2.2. EPI quantification methodology

A pixel's EPI can be derived by integrating the individual EPI contributions from the differential areas of the pixel GFOV (see upper subfigure in Fig. 3), which can be derived through the Eq. (1):

$$EPI^k = \sum_{i \in LGFOV} \cos(vz_i)\cos(\omega_i) A_i w^k P_i^k F_i^k \Big/ \left(\pi D_{Li}^2\right) \quad (1)$$

where the superscript k is set to be SW or LW, $LGFOV$ denotes the geolocation of the pixel GFOV. i denotes the center of a differential area within the pixel GFOV (The GFOV is discretized into the differential areas in 1° longitude × 1° latitude due to the TOA SW/LW flux data used in this study is in this spatial resolution). vz_i denotes the viewing zenith

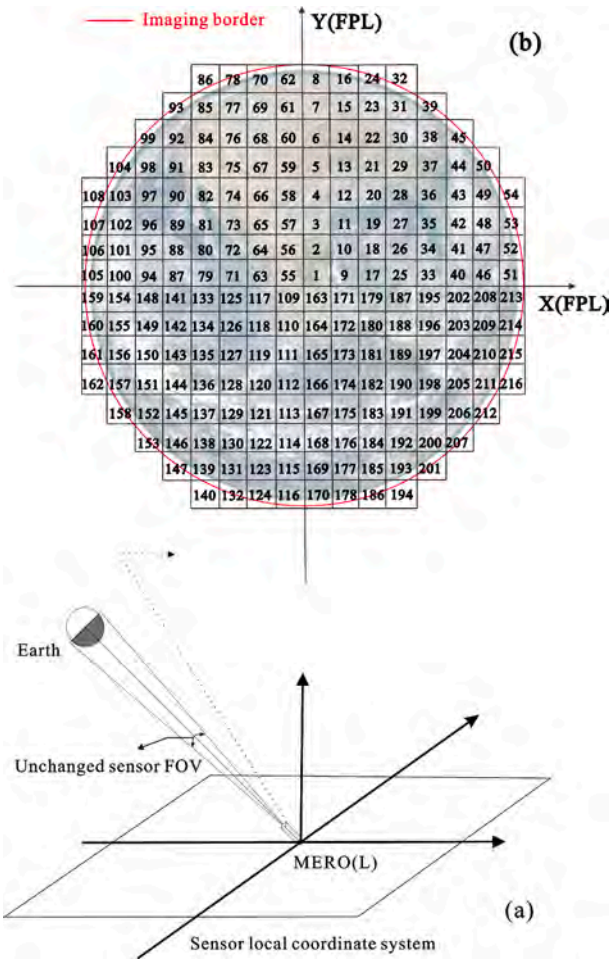

Fig. 2. (a) The unchanged MERO sensor FOV. (b) the correspondence between pixel location on the FPA and the pixel code number; the larger imaging border of the FPA than the actual image in most cases.

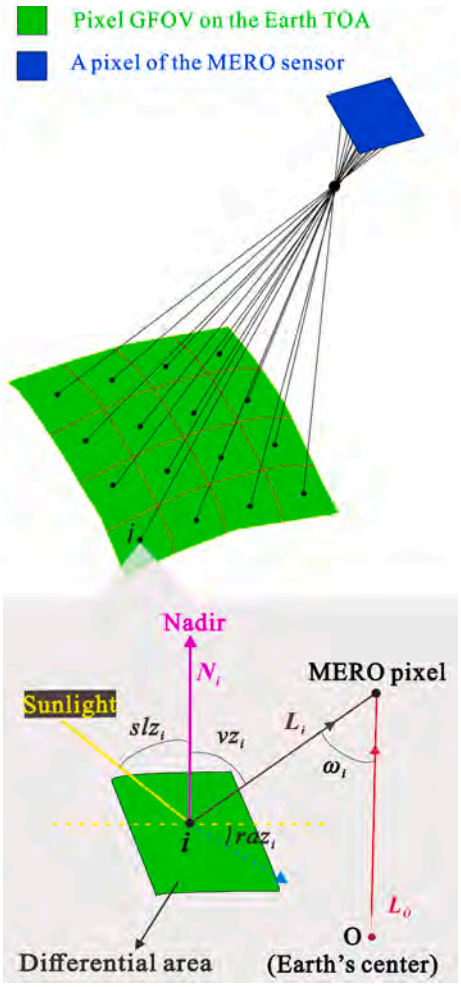

Fig. 3. The upper subfigure illustrates the pixel GFOV discretization. The bottom subfigure shows the partial parameters of the MERO-Earth geometry.

angle, ω_i is the *i*-Earth-center viewing difference angle, D_{Li} is the distance between the pixel and *i*, A_i is the area of *i* represents (see lower subfigure in Fig. 3 for the detailed geometric illustration of these parameters). w^{SW} and w^{LW} are the weight functions: w^{SW} is set to be 1 and 0 for sunlit and non-sunlit areas, respectively; w^{LW} is equal to 1 constantly; the reason for this definition of w^{SW} and w^{LW} is that the SW EPI is only contributed by the sunlit part of the GFOV while the LW EPI is contributed by both the sunlit and non-sunlit portions of the GFOV. The judgement of whether the area is sunlit can be made by the local solar zenith angle (slz_i). The above mentioned vz_i, ω_i, D_{Li}, A_i and slz_i are part of the MERO-Earth geometry. The *LGFOV* and MERO-Earth geometry can be derived through the pixel GFOV positioning method proposed in this study, which is described detailly below in section 2.2.1. P_i^{SW} and P_i^{LW} in Eq. (1) are the Earth TOA outgoing SW and LW anisotropy factors respectively, which determines directional radiance from the TOA flux. P_i^{SW} and P_i^{LW} can be derived from the TOA radiant anisotropy method proposed in this study, which is detailly exhibited in section 2.2.2. F_i^{SW} and F_i^{LW} in Eq. (1) are the TOA SW flux and TOA LW flux respectively, which can be derived from the CERES SYN 1-degree edition 4.1 dataset. This dataset is utilized owing to its high spatial-temporal resolution (up to 1° longitude × 1° latitude in spatial resolution and 1 h in temporal resolution) and relatively high accuracy (uncertainties in TOA SW and LW fluxes are <8 W/m^2 and <3 W/m^2, respectively)(Loeb 2017).

2.2.1. Pixel GFOV positioning method

This method has two main objectives, one is to locate the GFOV for every pixel, another is to derive the MERO-Earth geometry.

2.2.1.1. Pixel GFOV position derivation. Specifically, this objective is to derive the geolocation of the pixel GFOV (the middle blue quadrangle in the Fig. 4) in the Earth-centered Earth-fixed coordinate system (ECEF) based on the pixel's coordinates in the focal plane local coordinate system (FPL). The FPL is a two-dimensional orthogonal coordinate system fixed in the FPA with its origin located at the center of the FPA, which means that a pixel's FPL coordinates are unchanged (Fig. 4). The ECEF is a three-dimensional Cartesian coordinate system with the origin located at the Earth's center of mass. The X-axis points to the intersection of the prime meridian and the Earth's equator, the Z-axis points to the direction of the terrestrial North pole, and the Y-axis is perpendicular to the X-axis in right hand. In this study, the World Geodetic System-1984 (WGS-84) ellipsoid was used as the Earth geodetic datum. Since the ECEF would rotate towards the FPL due to Earth self-rotation, it is difficult to directly transform between the ECEF and FPL. Therefore, we used a transient Cartesian coordinate system (TC) to link the ECEF and FPL. The TC system had its origin at the origin of the ECEF system, and the Y–Z plane was parallel to the X–Y plane of the FPL system. The X-axis of the TC would always pass through the center of FPL due to that the MERO is angularly adjusted to ensure the sensor FOV center line passing through the Earth center (this would make the whole Earth disk always been observed by the MERO)(Duan et al. 2018). Consequently, the Y and Z coordinates of a pixel GFOV in TC could be derived by scaling up the X and Y coordinates of the pixel in the FPL whereby the Eq. (2):

$$\begin{pmatrix} Y_{TC} \\ Z_{TC} \end{pmatrix} = sca \begin{pmatrix} X_{FPL} \\ Y_{FPL} \end{pmatrix} \tag{2}$$

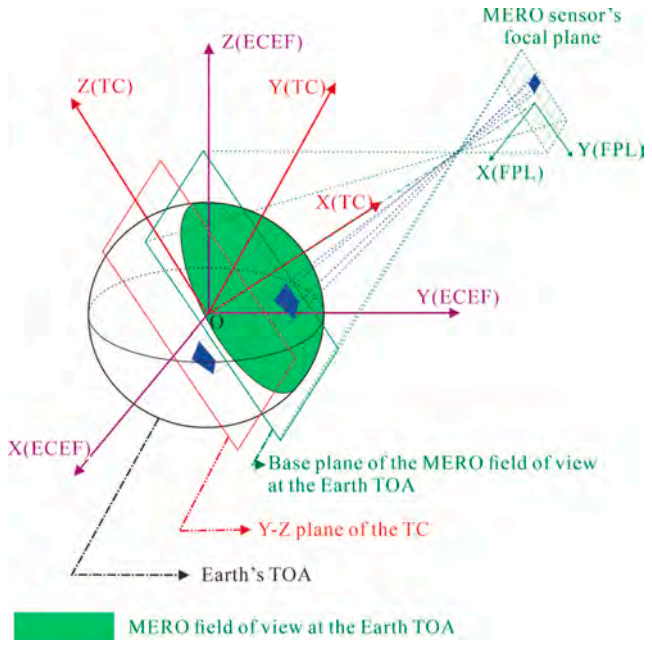

Fig. 4. The geometry of the focal plane local coordinate system (FPL) of a MERO, the transient Cartesian coordinate system (TC), and the Earth-centered Earth-fixed coordinate system (ECEF). From right to left, the three blue quadrangles represent a pixel in the focal plane, the pixel GFOV on the Earth TOA, and the pixel projection on the TC coordinate system, respectively. (For interpretation of the references to colour in this figure legend, the reader is referred to the web version of this article.)

where Y_{TC} and Z_{TC} are the Y and Z coordinates of a pixel GFOV in the TC, respectively, X_{FPL} and Y_{FPL} are the X and Y coordinates of the pixel in the FPL, respectively, and *sca* is the uniform amplifying factor, which is time-dependent and can be derived by Eq. (3):

$$sca = tan\left(\frac{IFOV}{2}\right)(D_{LE} - D_{BO})\frac{1}{64} \tag{3}$$

where *IFOV* is the unchanged sensor FOV, which is approximately 2.07°; D_{LE} is the distance between the center of the MERO's focal plane and the Earth center, which can be derived from multiplying the light speed by the variable "399_ins_LT" (the time taken for light to travel from the center of the Earth to the MERO); this variable can be derived from the Jet Propulsion Laboratory (JPL) HORIZONS ephemeris system. D_{BO} is the distance between the Y–Z plane of the TC and the base plane of the MERO field of view at the Earth TOA (Fig. 4); D_{BO} can be derived from Eq. (4):

$$D_{BO} = \frac{x_1y_2 - x_2y_1}{[y_2 - y_1 - tan\gamma(x_2 - x_1)]cos\gamma} \tag{4}$$

where (x_1, y_1) and (x_2, y_2) are the two solutions of the Eq. (5)

$$\begin{cases} \dfrac{x^2}{a^2} + \dfrac{y^2}{b^2} = 1 \\ (D_{LE}cos\gamma - x)\dfrac{x}{a^2} + (D_{LE}sin\gamma - y)\dfrac{y}{b^2} = 0 \end{cases} \tag{5}$$

where a and b are the major and minor semi-axes of the WGS-84 Earth TOA ellipsoid, respectively. γ is the central angle, which can be derived from Eq. (6):

$$\gamma = \theta_V - arcsin\left(\frac{ae^2 sin\theta_V cos\theta_V}{D_{LE}\sqrt{1 - e^2 sin^2\theta_V}}\right) \tag{6}$$

where θ_V is the WGS-84 latitude of the sub-MERO point, which can be derived from the variable "sub-MERO-latitude" generated by JPL HORIZONS; e is the first eccentricity of the WGS-84 Earth TOA ellipsoid. Once Y_{TC} and Z_{TC} are derived, X_{TC} can be obtained by solving the Eq. (7):

$$\begin{cases} \dfrac{X_{ECEF}^2}{a^2} + \dfrac{Y_{ECEF}^2}{a^2} + \dfrac{Z_{ECEF}^2}{b^2} = 1 \\ \begin{bmatrix} X_{ECEF} \\ Y_{ECEF} \\ Z_{ECEF} \end{bmatrix}^T = \begin{bmatrix} X_{TC} \\ Y_{TC} \\ Z_{TC} \end{bmatrix}^T \begin{bmatrix} cos\gamma & 0 & sin\gamma \\ 0 & 1 & 0 \\ -sin\gamma & 0 & cos\gamma \end{bmatrix} \begin{bmatrix} cos\varphi_V & sin\varphi_V & 0 \\ -sin\varphi_V & cos\varphi_V & 0 \\ 0 & 0 & 1 \end{bmatrix} \end{cases} \tag{7}$$

where φ_V is the WGS-84 longitude of the sub-MERO point, which can be derived from the variable "sub-MERO longitude" generated by JPL HORIZONS. After $[X_{TC}\ Y_{TC}\ Z_{TC}]$ is obtained, the ECEF coordinates of the pixel GFOV, i.e., $[X_{ECEF}\ Y_{ECEF}\ Z_{ECEF}]$ could be derived by Eq. (7).

2.2.1.2. MERO-Earth geometry derivation. The MERO-Earth geometry could be derived by the pixel-GFOV positioning method with the help of JPL HORIZONS ephemeris system. Hereafter we will show derivation of the MERO-Earth geometric variables that used in this study (mainly used in Eq. (1)).

The viewing zenith angle vz_i can be derived from Eq. (8):

$$vz_i = \arccos\frac{\boldsymbol{L}_i \cdot \boldsymbol{N}_i}{|\boldsymbol{L}_i||\boldsymbol{N}_i|} \tag{8}$$

where $\boldsymbol{L}_i$ is the viewing vector from i (center of a differential area within the pixel GFOV) pointing to the pixel (detector unit) (see bottom subfigure of Fig. 3), which can be derived from the Eq. (9):

$$\boldsymbol{L}_i = \begin{bmatrix} D_{LE}cos\gamma cos\varphi_V - X_{ECEF_i} \\ D_{LE}cos\gamma sin\varphi_V - Y_{ECEF_i} \\ D_{LE}sin\gamma - Z_{ECEF_i} \end{bmatrix}^T \tag{9}$$

$\boldsymbol{N}_i$ (the normal vector) can be obtained using Eq. (10):

$$\boldsymbol{N}_i = \begin{bmatrix} \dfrac{X_{ECEF_i}}{a^2} & \dfrac{Y_{ECEF_i}}{a^2} & \dfrac{Z_{ECEF_i}}{b^2} \end{bmatrix} \tag{10}$$

A_i (the size of the differential area that i represents) can be derived by the ellipsoidal integration.

D_{Li} (the MERO-i distance) can be derived by the norm of vector $\boldsymbol{L}_i$. ω_i (the i-Earth-center viewing difference angle) could be derived from Eq. (11):

$$\omega_i = \arccos\frac{\boldsymbol{L}_i \cdot \boldsymbol{L}_O}{|\boldsymbol{L}_i||\boldsymbol{L}_O|} \tag{11}$$

Where $\boldsymbol{L}_O$ (the Earth-center viewing vector) can be derived from Eq. (12):

$$\boldsymbol{L}_O = \begin{bmatrix} D_{LE}cos\gamma\ cos\varphi_V \\ D_{LE}cos\ \gamma sin\varphi_V \\ D_{LE}sin\gamma \end{bmatrix}^T \tag{12}$$

slz_i (solar zenith angle) can be derived from Eq. (13):

$$slz_i = arccos\left(\frac{\boldsymbol{S} \cdot \boldsymbol{N}_i}{|\boldsymbol{S}||\boldsymbol{N}_i|}\right) \tag{13}$$

Where $\boldsymbol{S}$ (the solar position vector) can be derived from Eq. (14)

$$\boldsymbol{S} = [\,cos\theta_S cos\varphi_S \quad cos\theta_S sin\varphi_S \quad sin\theta_S\,] \tag{14}$$

where θ_S and φ_S are the WGS-84 latitude and longitude of the sub-solar point, respectively, which can be derived from the JPL HORIZONS generated variables "sub-solar latitude" and "sub-solar longitude", respectively.

2.2.2. Earth TOA radiant anisotropy method

The Earth TOA SW and LW outgoing directional radiance is not

isotropic at every direction, which depend not only on the viewing geometry, but also on the cloud conditions, the type of the surface beneath the area at the TOA, and several cloud and meteorological factors, due to that the Earth surface reflect the solar radiation and emit the longwave radiation anisotropically and that the cloud absorption, reflection and emittance are not isotropic (Nagol et al. 2015). Here we use the anisotropic factor ($I\pi/F$, where I is the directional radiance, F is the TOA flux) to detailly characterized the TOA radiant anisotropy and determine the directional radiance from the TOA flux to calculate the MERO pixel-scale EPI. In this study, the anisotropic factors are generated by the TOA radiant anisotropy method with full consideration of the influences from the viewing geometry, the related cloud and meteorological factors and the surface type. Note that the TOA radiant anisotropy method proposed in this study is constructed by referring to the CERES Angular Distribution Models (ADMs) (Loeb et al. 2005; Loeb et al. 2003; Su et al. 2015). Since the TOA SW and LW anisotropy methods depend on different factors, hereafter we will describe them separately.

2.2.2.1. TOA SW anisotropy method. The factors that affect the TOA SW anisotropy are shown in Table 1, which mainly includes the surface type (ocean, land or snow), the related cloud and meteorological factors (wind speed, cloud type, cloud fraction and optical depth) and the viewing geometry (solar zenith, viewing zenith and relative azimuth angles). To generate the anisotropic factor with fully consideration of these factors, we used the scene type approach (Su et al. 2015): the TOA SW anisotropy method is a set of one-scene-type-to-one-anisotropic-factor correspondences, once the scene type is determined, the TOA SW anisotropic factor is derived. The SW scene type is a form of combination of the influencing factors listed shown in Table 1, which is detailly constructed by following steps. 1. Every of the influence factor is discretized into several bins, for example, wind speed is discretized into 4 bins (see Table 1). 2. Then a scene type is formed by a possible combination of the bins corresponding to all of the influencing factors respectively. For example, scene type No. 1 is a combination of the following factor bins: 1. surface type bin: ocean, 2. cloud condition bin: clear, 3. wind speed bin: < 3.5 m s^{-1}, 4. solar zenith angle bin: 0°–10°, 5. relative azimuth angle bin: 0°–10°, and 6. viewing zenith angle, 0°–10°. Other scene types, such as scene type No.2, No.3, No.100, could be constructed by the same way. Afterwards, the SW anisotropic factor corresponding to each scene type could be derived though the CERES ADMs and the CERES Single Scanner Footprint (SSF) dataset. To determine the SW anisotropic factor for a certain TOA area at a certain time when calculating the pixel-scale EPI, the values of the influencing factors listed in Table 1 should be derived through certain datasets to finally determine the SW scene type: the surface type could be determined through the CERES surface type data or the NOAA JPSS-VIIRS (joint polar satellite system-visible infrared imaging radiometer suite) surface type data; the cloud and meteorological factors, such as the wind speed, cloud type, cloud fraction, and optical depth, can be derived from the CERES SYN and CldTypHist datasets; cloud condition could be determined by the judgement of cloud fraction (>0.1% means cloudy, the else means clear); the viewing geometry factors could be derived by the pixel GFOV positioning method illustrated above.

2.2.2.2. TOA LW anisotropy method. Unlike the TOA SW anisotropy, the TOA LW anisotropy is irrelevant to the solar zenith and relative azimuth angles, but sensitive to other factors, such as the precipitable water, the cloud emissivity and the vertical temperature change (VTC). VTC under clear sky condition can be calculated by subtracting the air temperature at the location where the pressure is 300 hPa lower than the surface pressure from the surface skin temperature. Under cloudy condition, the VTC can be derived by subtracting the effective cloud temperature from the underlying surface skin temperature. Detailed information about the factors that influence the LW anisotropy are listed in the Table 2. The TOA LW anisotropy method is constructed in the same way as the TOA SW anisotropy method. All the values of the influencing factors listed in Table 2 for determining LW scene type can be derived through the same datasets that are used in the SW scene type determination.

3. Methodological improvements made in this study

As indicated above, the pixel-scale EPI quantification involves 3 major parts: the "absolute" Earth TOA flux of known accuracy, the pixel GFOV positioning method, and the Earth TOA radiant anisotropy method. Compared to our previously 2 published EPI researches (Duan et al. 2019; Duan and Jin 2019), this study mainly makes vital improvements to the latter two components.

3.1. Improvement in the pixel GFOV positioning method

The GFOV positioning method proposed in our firstly published EPI study is made for the wide-field-of-view single-detector MERO sensor where the GFOV is the whole Earth disk (Duan et al. 2019). This method definitely cannot be used for the multi-pixel (detector unit) MERO sensor due to that the pixel GFOV positioning involving projecting the pixel shape in the focal plane local coordinate system (FPL) on the Earth

Table 1
Factors that influence the TOA SW anisotropy and their discretized bins used to construct the SW scene type.

Surface type	Cloud condition	Cloud and meteorological factors	Viewing geometry
ocean	1) clear 2) cloudy	1) clear condition only: a. wind speed (4 bins: < 3.5, 3.5–5.5, 5.5–7.5, > 7.5 m s^{-1}) 2) cloudy conditions only: b. cloud type (2 bins: liquid water cloud or ice cloud) c. cloud fraction (12 bins: 0.1%–10%, 10%–20%, 20%–30%, 30%–40%, 40%–50%, 50%–60%, 60%–70%, 70%–80%, 80%–90%, 90%–95%, 95%–99.9%, 99.9%–100%) d. optical depth (14 bins: 0–1, 1–2.5, 2.5–5, 5–7.5, 7.5–10, 10–12.5, 12.5–15, 15–17.5, 17.5–20, 20–25, 25–30, 30–40, 40–50, >50)	1) solar zenith angle (9 bins: 0°–90°in step of 10°) 2) relative azimuth angle (10 bins: 0°–10°, 10°–170°in step of 20°, 170°–180°) 3) viewing zenith angle (9 bins: same as the solar zenith angle)
land and desert	1) clear 2) cloudy	cloudy conditions only: a. cloud type (2 bins: liquid water cloud or ice cloud) b. cloud fraction (5 bins: 0.1%–25%, 25%–50%, 50%–75%, 75%–99.9%, 99.9%–100%) c. optical depth (6 bins: 0–2.5, 2.5–6, 6–10, 10–18, 18–40, > 40)	1) solar zenith angle (9 bins: same as the ocean) 2) relative azimuth angle (10 bins: same as the ocean) 3) viewing zenith angle (9 bins: same as the ocean)
snow	1) clear 2) cloudy	cloudy conditions only: a. cloud fraction (5 bins: 0.1%–25%, 25%–50%, 50%–75%, 75%–99.9%, 99.9%–100%) b. optical depth (2 bins: ≤10, >10)	1) solar zenith angle (45 bins: steps of 2° from 0° to 90°) 2) relative azimuth angle (10 bins: same as the ocean) 3) viewing zenith angle (9 bins: same as the ocean)

Table 2
Factors that influence the TOA LW anisotropy and their discretized bins used to construct the LW scene type.

Surface type	Sunlit condition	Cloud condition	Cloud and meteorological factors	Viewing geometry
ocean	1) day 2) night	1) clear 2) cloudy	for both clear and cloudy conditions: a. precipitable water (3 bins: < 33%, 33%–66%, > 66%) b. vertical temperature change (4 bins: < 25%, 25%–50%, 50–75%, > 75%) for cloudy conditions only: a. cloud fraction (5 bins: 0.1%–25%, 25%–50%, 50%–75%, 75%–99.9%, 99.9%–100%) b. cloud emissivity (4 bins: < 25%, 25%–50%, 50%–75%, > 75%)	viewing zenith angle (9 bins: 0°–90°in step of 10°)
land and desert	1) day 2) night	1) clear 2) cloudy	same as the ocean	viewing zenith angle (9 bins: same as the ocean)
snow	1) day 2) night	1) clear 2) cloudy	for both clear and cloudy conditions: a. vertical temperature change (2 bins: < 20 K, ≥ 20 K) b. surface skin temperature day (2 bins: < 250 K, ≥ 250 K) night (2 bins: < 240 K, ≥ 240 K) for cloudy conditions only: a. cloud fraction (5 bins: same as the ocean)	viewing zenith angle (9 bins: same as the ocean)

TOA in the Earth-centered fixed coordinate system (ECEF), which is totally unnecessary in our firstly published EPI study (the GFOV positioning method in our firstly published EPI study just involves the ECEF coordinates of the sub-MERO point). Therefore, we proposed a preliminary pixel GFOV positioning method in our secondly published EPI study (Duan and Jin 2019), which is a compromised way that didn't directly conduct the projection and coordinate transformation mentioned above. The rationale of this preliminary pixel-scale GFOV positioning method is to finding the regular Earth girds within the pixel GFOV (the globe is regularly discretized; every grid represents a fixed 1° longitude × 1° latitude area), then the combination of the fixed Earth TOA areas corresponding to the found Earth grids is set as the method determined pixel GFOV. However, such a method produced GFOV would be evidently different from the actual GFOV in most cases (see Fig. 5); this would introduce obvious uncertainty in the EPI quantification since the highly spatial variabilities of the TOA radiant flux and the anisotropy as well as viewing geometry. The main reason for this mismatch is comprised of two parts; the first is the lunar libration that would bring a rotational movement to the MERO viewing geometry towards Earth; the second is that the distribution of these found Earth grids in the actual GFOV is irregular (see Fig. 5).

To overcome this defect of our secondly published EPI research, we proposed a new pixel GFOV positioning method based on projection in this study. This method works as follows. As show in Fig. 4, the detector unit (pixel) is firstly projected on the Z-X plane of the TC coordinate system into the shape projection function (P_{TC}); Then P_{TC} is projected on the ellipsoidal Earth TOA into the shape function (P_{ECEF}) in the ECEF coordinates. Afterwards, P_{ECEF} is set as the method determined pixel GFOV and then finally participate in the EPI calculation. In this approach, the finally method determined pixel GFOV (P_{ECEF}) would always be the pixel's actual projection on the Earth TOA with the bridging function of the intermediate projection P_{TC}, that is, the method determined pixel GFOV would always fully consistent with the actual pixel GFOV. This could substantially reduce the uncertainties induced by the mismatch. To quantitatively show the accuracy enhancement brought by this improvement, we make two separate calculations of the annual mean EPI over 2019 using the pixel GFOV positioning method of our secondly published EPI research and utilizing that of this study respectively. Note that these two computations are conducted based on the same EPI quantification method proposed in this study except for the pixel GFOV positioning methods. Show in Fig. 6 is the results comparison, it is indicated that the accuracy enhancement in SW EPI approximates as high as 66.80% for certain pixel and the average accuracy improvement is 7.79% (Fig. 6 (b)). While the accuracy enhancement in LW EPI is slightly weaker, the maximum and averaged improvements are about 38.50% and 3.84%, respectively (Fig. 6 (d)).

3.2. Improvements in the TOA radiant anisotropy method

In our firstly published EPI study, the TOA SW radiant anisotropy is not considered and the LW radiant anisotropy method is oversimplified without consideration of the effects from related cloud and meteorological parameters. Therefore, we utilized a modified TOA SW radiant anisotropy method in our secondly published EPI study with partial consideration of the effect from viewing geometry (the solar zenith and viewing zenith angles). However, such a slightly modified TOA SW anisotropy method still didn't take into account the vital influences from the surface type, the related cloud and meteorological parameters (cloud type, cloud fraction, optical depth, etc.); this would neglect the actual variability of the TOA SW anisotropic factors. For example, exhibited in Fig. 7 (a) are the TOA SW anisotropic factors utilized in our secondly published EPI study (black line) and the TOA SW anisotropic factors under different cloud and meteorological parameters and surface types utilized in this study (2 red lines) at the same viewing geometry (solar zenith angle: 0°-10°, relative azimuth angle: 30°-50°); it is clearly showed that the SW anisotropy method of our secondly published EPI

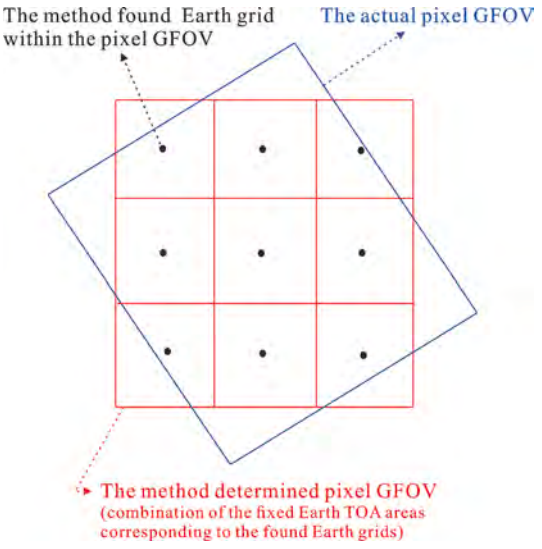

Fig. 5. The mismatch between the method determined GFOV and the actual GFOV in our secondly published EPI study.

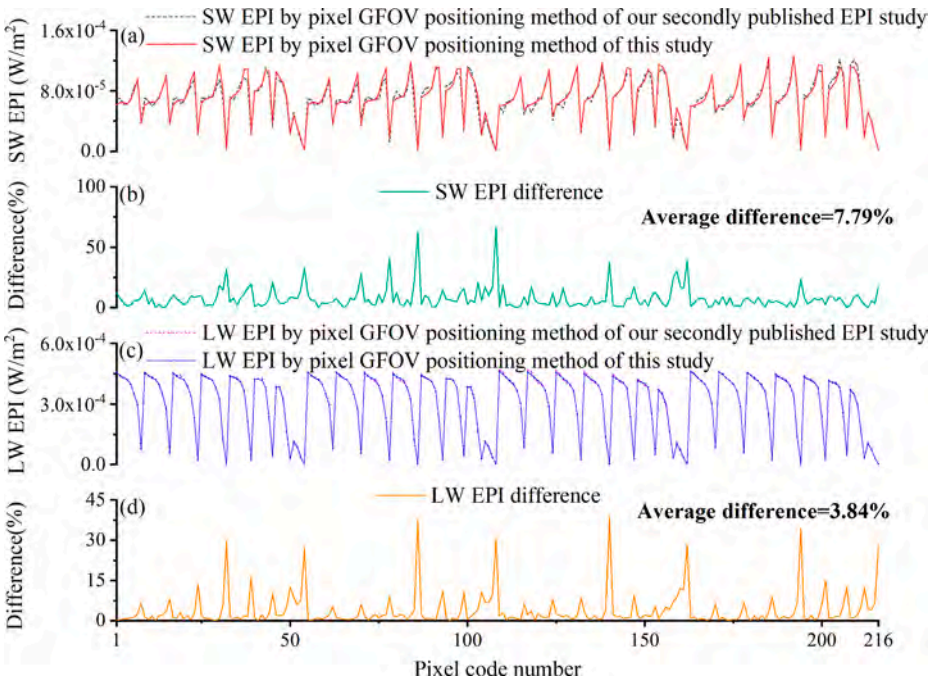

Fig. 6. (a) Results of annual mean SW EPI of 2019 for every pixel using the pixel GFOV positioning method of our secondly published EPI study and utilizing that of this study, respectively; (b) difference between these two SW EPI results; (c) results of annual mean LW EPI of 2019 for every pixel using the pixel GFOV positioning method of our second published EPI study and using that of this study, respectively; (d) difference between these two LW EPI results.

study (black line) would definitely neglect the SW anisotropic factor variability caused by the change of the related meteorological factors (cloud fraction and optical depth) and surface type variation (ocean and land) (2 red lines). Furthermore, the TOA LW anisotropy method used in our secondly published EPI study still remains the oversimplified one of our firstly published EPI research (black line in Fig. 7 (b)), which also neglect the effect from the variation of the related cloud/meteorological parameter and did not distinguish the land and ocean surface types (2 red lines in Fig. 7 (b)). In all, through our secondly published EPI study make certain improvements in terms of the TOA SW anisotropy compared to our firstly published EPI work, either the SW or LW anisotropy method used in our secondly published EPI study is still remarkably inaccurate, which would lead to evident uncertainty in the pixel-scale EPI quantification.

To overcome these drawbacks, we fully upgrade the TOA SW and LW anisotropy methods in this study by sufficiently considering their close dependence on the related factors, such as surface type, the cloud and meteorological parameters and the viewing geometry (details of these factors are shown in Tables 1 and 2). To exhibit the significance of the TOA radiant anisotropy improvements made in this study, we made a quantitative comparison between the TOA radiant anisotropy method of this study and that of our secondly published EPI work by calculating the annual mean EPI of 2019 for every pixel. Note that these two calculations used the same EPI quantification method proposed in this study except that the utilized TOA radiant anisotropy methods are different. The evaluation results are shown in Fig. 8, it is indicated that the accuracy improvement of certain pixel could reach 138.09% for SW EPI quantification (Fig. 8 (b)) and 43.44% for LW EPI computation (Fig. 8 (d)); the average accuracy enhancement for pixel-scale SW EPI quantification is 20.67%, while the average accuracy improvement for pixel-scale LW EPI quantification is 12.15%. This implies the TOA radiant anisotropy method enhancements of this study could substantially improve the accuracy of both the pixel-scale SW and LW EPI quantifications.

4. Results of 18.6-year pixel-scale EPI variability prediction

As indicated in Eq. (1), EPI variability should be driven by the MERO-Earth geometry evolution, the anisotropic factor variation, and the Earth TOA flux change. Despite these, the MERO location on the Moon would also have certain consequences for the EPI variability. Separate assessments of influences from these driving factors on the EPI change and the after integration of their results could efficiently reveal the future long-term pixel-scale EPI change. However, as indicated in section 2.2.2 and Tables 1 and 2, the anisotropic factor change is closely related to the MERO-Earth geometry change; solely evaluating the variability of anisotropic factor on EPI variation would overlap with that of the MERO-Earth geometry. Therefore, we have integrated such assessments for the anisotropic factor and MERO-Earth geometry. The 18.6-year range is chosen as the evaluating period due to that it is the longest subfactor variation period (18.6 years period of the Moon's orbital inclination variation, named as the lunar standstill cycle, which belongs to the MERO-Earth geometry variation).

4.1. Influence from MERO-Earth geometry temporal variation and anisotropic factor temporal change

In this evaluation, a temporal variation mode of the TOA anisotropic-factor-dominant factors (see Table 1 and Table 2 for details of these factors) is set in the calculation of the EPI variability caused by the MERO-Earth geometry temporal change; therefore, the derived results could reflect the influence from both the anisotropic factor variation and the MERO-Earth geometry change since the anisotropic factor participate in this EPI variability computation. The TOA anisotropic-factor-dominant factors temporal variation mode is detailly defined as follows: 1. for the related cloud and meteorological factor (such as the optical depth, the cloud fraction), the future 18.6 year change is set to be as same as the variation occurs in the past 18.6 years, that is, the annual variability of 2019 is the basic, the 2020 variability is derived by the 2019 variability plus the interannual change between 2001 and 2002; this is a conservative assumption, which can be improved by the CMIP (Coupled Model Intercomparison Project) 6 projections in the future; 2.

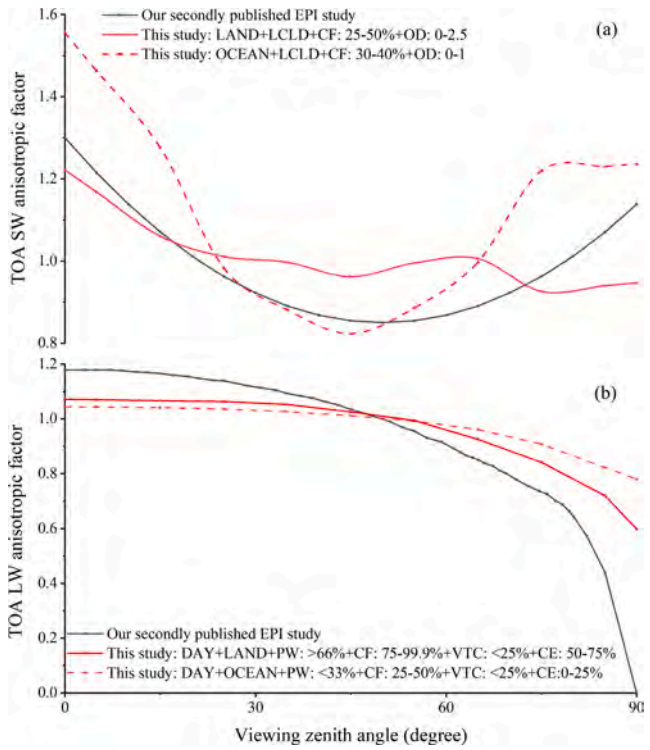

Fig. 7. (a) Comparison of the oversimplified TOA SW anisotropic factor used in our secondly published EPI study (black line) and the more realistic TOA SW anisotropic factors under different cloud/meteorological parameter bins and surface types utilized in this study (2 red lines); LCLD represents the liquid cloud, CF represents the cloud fraction, OD represents the optical depth; (b) comparison of the oversimplified TOA LW anisotropic factor for non-snow surface type used in our secondly published EPI study (black line) and the more realistic TOA LW anisotropic factors under different cloud/meteorological parameter bins and surface types (land and ocean) utilized in this study (2 red lines), PW represents the precipitable water, CF represents the cloud fraction, VTC represents the vertical temperature change, CE represents the cloud emissivity. (For interpretation of the references to colour in this figure legend, the reader is referred to the web version of this article.)

the surface type change is not considered in this study, which would keep the same during the future 18.6 years (March 2019 to November 2037). To effectively evaluate the influence from the MERO-Earth geometry variation and anisotropic factor change, it is necessary to assume that the other two factors—the Earth TOA fluxes and the MERO location—are temporally invariant. We therefore set the monthly mean TOA SW and LW fluxes of March 2019 as these invariant TOA fluxes for the reason that these monthly means could ensure values of the SW flux from anywhere on the globe to be available. Such a setting could make the pixel-GFOV sunlit portion (the location is temporally varying) has a correct non-zero TOA SW flux. In contrast, if the instantaneous global TOA SW and LW fluxes are set as these invariant TOA fluxes, half of the globe in fixed location would have zero-value TOA SW fluxes; this could lead to a case that a pixel-GFOV sunlit portion (the location is temporally varying) may has an incorrect zero TOA SW flux when this sunlit portion overlap with the above fixed-located half globe (having zero-value TOA SW fluxes). Such a case would introduce remarkable uncertainty to the assessment. To eliminate the influence from the MERO selenographic location change, we set the invariant MERO location to be the origin of the selenographic coordinate system (i.e., 0°, 0°).

Fig. 9 shows the results of the SW EPI variations induced by MERO-Earth geometry variation and anisotropic factor change over the future 18.6 years (March 2019 to November 2037). For a given pixel, the upper and lower bounds of the variation shown in Fig. 9 (a) were calculated by subtracting the monthly mean EPI of March 2019 shown in Fig. 9 (c) from the maximum and minimum of the monthly mean EPIs between March 2019 and November 2037, respectively. We chose March 2019 as the basis because this month was the beginning of the assessment period and the monthly mean TOA fluxes of this month were used as the invariant global TOA fluxes in the assessment. Note that, the monthly mean SW and LW EPIs of March 2019 of MERO located at the origin of the selenographic coordinate system-(0°, 0°) were also set as the basis in the following evaluations for consistency, so we hereafter name it as the overall basis. We consider that the common use of this overall basis and the relative values (upper bound and lower bound) in all of the separate influence evaluations is necessary for the final integration of all the assessment results. Fig. 9 also shows that the largest SW EPI variability (the SW EPI upper bound minus the lower bound) would occur at high pixels, such as pixels 7, 15, 23, and 31. We consider the most plausible reason for this to be that these border pixels are concentrated in high-latitude areas of the Earth, where the extreme polar day (pixel-GOFV is totally sunlit, upper bound SW EPI occurs) and polar night (pixel-GOFV is totally dark, lower bound EPI occurs) seasons would make the variation range (upper bound minus lower bound) much larger. The smallest SW EPI variability mainly occurs at certain border pixels, such as pixels 32 and 54, this is due to that these border pixels mainly face the outer space instead of the Earth (see Fig. 2 (b)); which is caused by the unchanged sensor FOV that makes the imaging border larger than the actual whole Earth disk. Fig. 10 indicate that the largest variability (upper bound minus lower bound) in the LW EPI mainly occurs at middle pixels, such as pixels 4, 12, and 20 (see Fig. 2 (b) for the correspondence between pixel location on the FPA and the pixel code number). We consider the most plausible reason for this to be that the LW EPI variability is primarily governed by the TOA LW flux variability in the pixel GFOV. For example, location of the GFOV corresponding to pixel 4 (pixel 4 has the largest LW EPI variability) varies from the near-equatorial zone (latitude of 1.43°) to the near-polar region (latitude of 58.57°) over the 18.6-year assessment period, which leads to a much larger TOA LW flux variability in the GFOV of pixel 4. The minimum LW EPI variability mainly occurs at certain border pixels such as pixels 32 and 54, where the smallest SW EPI variability also appears, due to that these pixels primarily "look" the outer space instead of the Earth (see Fig. 2 (b)).

4.2. *Influence from TOA flux temporal change*

This assessment is divided into two steps: 1. an evaluation of the pixel-scale-EPI versus TOA-flux sensitivity; 2. a TOA flux long-term variability prediction.

4.2.1. *Sensitivity of the pixel-scale EPI to the Earth TOA flux*

This sensitivity can be derived by averaging instantaneous ratios ($\Delta EPI/\Delta F$, where ΔEPI is the transient EPI variation, ΔF is the Earth TOA flux change) over the assessment period (March 2019 to November 2037). To eliminate the influences from the anisotropic factor temporal change in this assessment, we set the TOA anisotropic-factor-dominant factors (such as the optical depth, the cloud fraction) to be temporally invariant as the monthly mean of March 2019. To eliminate the influence from the MERO selenographic location, we set the MERO location to be invariant (the origin of the selenographic coordinate system (i.e., 0°, 0°)). Note that the MERO-Earth geometry temporal change would also have consequences in this assessment mainly through two subfactors: pixel-GFOV solid angle and the pixel GFOV size. Accordingly, we utilized a geometric correction coefficient (GCC) to eliminate the effects from these two MERO-Earth geometry subfactors, GCC can be derived from the Eq. (15):

$$GCC_i = \frac{\overline{A_i} D_i^2}{A_i \overline{D_i^2}} \tag{15}$$

where $(D_i/\overline{D_i})^2$ was used to correct the solid angle effect and $\overline{A_i}/A_i$ was

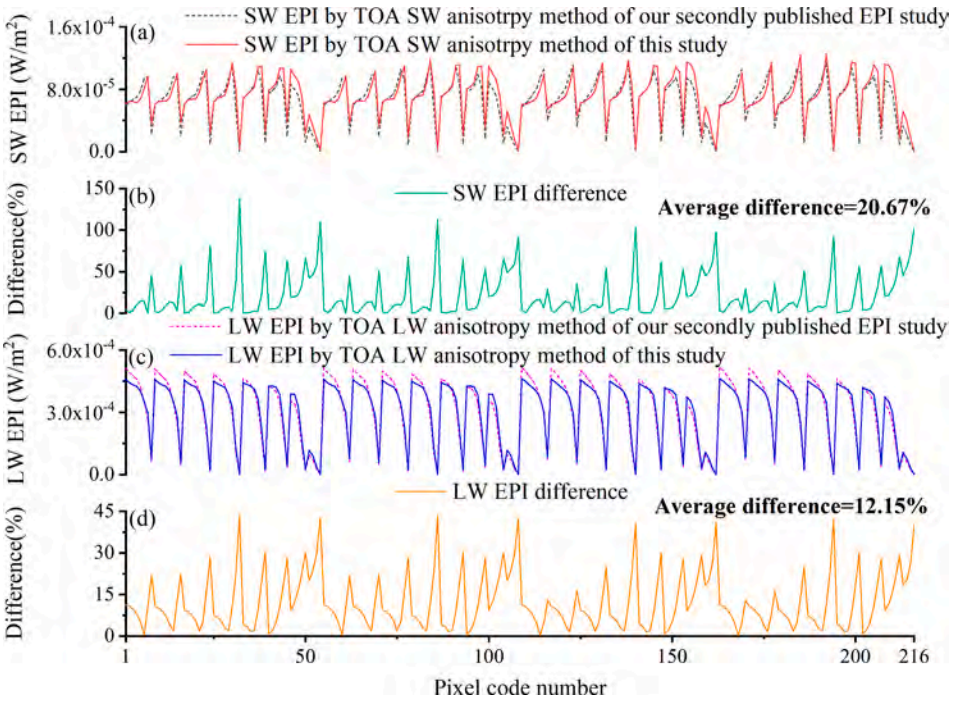

Fig. 8. (a) Results of annual mean SW EPI of 2019 for every pixel using the oversimplified TOA SW anisotropy method of our secondly published EPI study and using the more realistic TOA SW anisotropy method of this study, respectively; (b) difference between these two SW EPI results; (c) results of annual mean LW EPI of 2019 for every pixel using the oversimplified TOA LW anisotropy method of our secondly published EPI study and using the more realistic TOA LW anisotropy method of this study, respectively; (d) difference between these two LW EPI results.

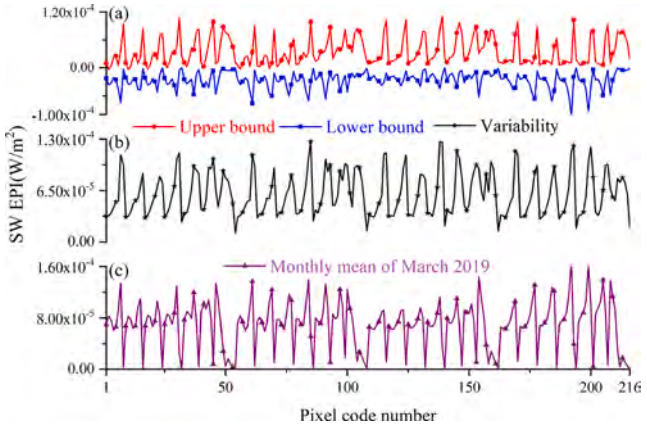

Fig. 9. SW EPI variation induced by the MERO-Earth geometry temporal change and SW anisotropic factor temporal variation over the 18.6-year period from March 2019 to November 2037 for each pixel. (a) the SW EPI upper bound and lower bound relative to the monthly mean SW EPI of March 2019 of MERO located at (0°, 0°) (selenographic coordinates); (b) the variability (upper bound minus lower bound), and (c) the monthly mean SW EPI of March 2019 of MERO located at (0°, 0°), which is set as the overall SW EPI basis in all stages of the prediction.

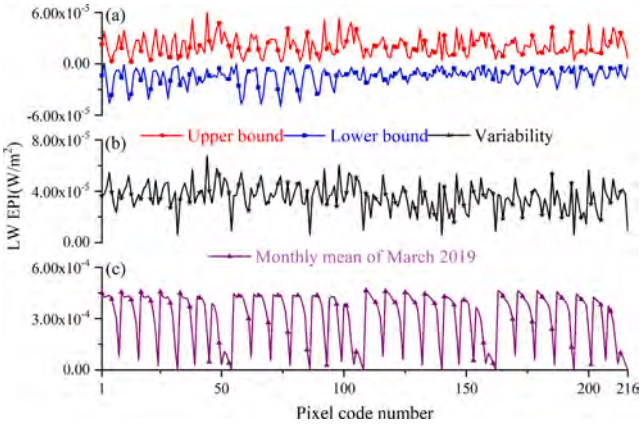

Fig. 10. LW EPI variation induced by the MERO-Earth geometry temporal change and LW anisotropic factor temporal variation over the 18.6-year period from March 2019 to November 2037 for each pixel. (a) the LW EPI upper bound and lower bound relative to the monthly mean LW EPI of March 2019 of MERO located at (0°, 0°) (selenographic coordinates); (b) the variability (upper bound minus lower bound), and (c) the monthly mean LW EPI of March 2019 of MERO located at (0°, 0°), which is set as the overall LW EPI basis in all stages of the prediction.

used to correct the GFOV size effect. D_i is the distance between pixel i and the center of the pixel GFOV, $\overline{D_i}$ is the temporal average of D_i.

Afterwards, the sensitivity (*SEF*) of pixel-scale EPI to Earth TOA flux could be derived through Eq. (16):

$$SEF_i = \frac{1}{N}\sum_{j=1}^{N} GCC_i^j \frac{\Delta EPI_i^j}{\Delta F_i^j} \tag{16}$$

where N is the number of temporal samples, ΔF_i^j is the TOA flux variation at temporal sampling j, and ΔEPI_i^j is the induced EPI change. Fig. 11 shows the *SEF* of each pixel over the 18.6-year assessment period (March 2019 to November 2037). For most pixels, the LW sensitivity is larger than the SW sensitivity. We think the most plausible reason for this to be that all of the pixel GFOV contributes to the LW EPI whereas the SW EPI only depend on the sunlit part of the pixel GFOV. There is a symmetry between different quadrants in terms of both the SW and LW sensitives. For example, the SW/LW EPI sensitivities of the pixels in quadrant 1 (pixels 1–54) are symmetric to those of the pixels in quadrant 2 (pixels 55–108), and are also symmetric to those of the pixels in quadrant 3 (pixels 109–162) and in quadrant 4 (pixels 163–216). We think this is attributed to the fact that there is a symmetry in terms of the viewing geometry of these pixels. Furthermore, there is an increasing trend in the SW EPI sensitivity from the central pixels to the near border pixels—e.g., pixels 1 to 7 (Fig. 11 (a)). We consider this may be due to that the SW EPI sensitivity is mainly positively correlated to the proportion of sunlit part in the pixel GFOV; the near border pixel GFOV is mainly located at high latitudes on Earth, when it is at the polar day

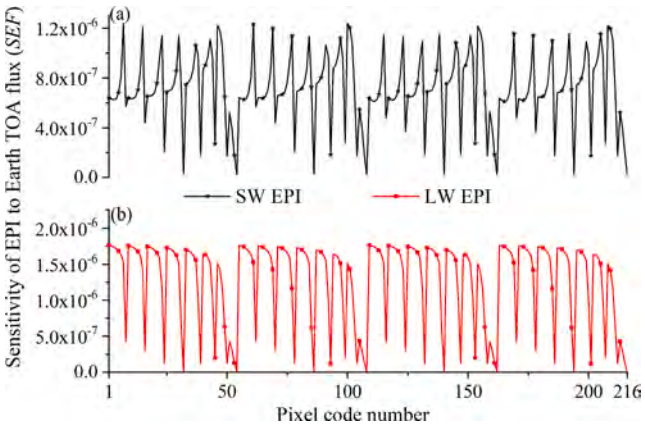

Fig. 11. (a) Sensitivity of the pixel-scale SW EPI to the Earth TOA SW flux and (b) sensitivity of pixel-scale LW EPI to the Earth TOA LW flux.

season, the entire pixel GFOV would be sunlit; whereas the central pixel doesn't have such a chance. By contrast, the LW EPI sensitivity tends to decrease from the center pixel to near boundary pixel (Fig. 11 (b)). We consider the most plausible reason for this to be that the LW EPI sensitivity primarily positively correlate to the TOA LW anisotropy factor, which is negatively related with the viewing zenith angle (Fig. 7 (b)) and the central pixels have smaller viewing zenith angles than the boundary pixels.

4.2.2. Earth's SW/LW TOA flux long-term variability prediction

The CERES mission has produced a continuous time series of the Earth TOA outgoing SW and LW fluxes since March 2000 (Fig. 12). It is indicated that although the globe experienced substantial influences from natural and anthropogenic activities during the past 19 years, either the TOA SW or LW interannual variability is relatively small and stable. Accordingly, we consider that it is acceptable to assume the future 18.6 years TOA flux interannual change to be the same with that of the past 18.6 years. Under such an assumption, the TOA SW flux over the future 18.6-year assessment period (March 2019 to November 2037) is projected to vary from −5.78 to 11.88 W/m^2 relative to the TOA SW flux of March 2019 (97.19 W/m^2); while the TOA LW flux over the same assessment period would fluctuate between −2.74 and 5.95 W/m^2 relative to the TOA LW flux of March 2019 (238.86 W/m^2).

4.2.3. EPI variability induced by TOA flux change

EPI variability induced by TOA flux change for every pixel during the

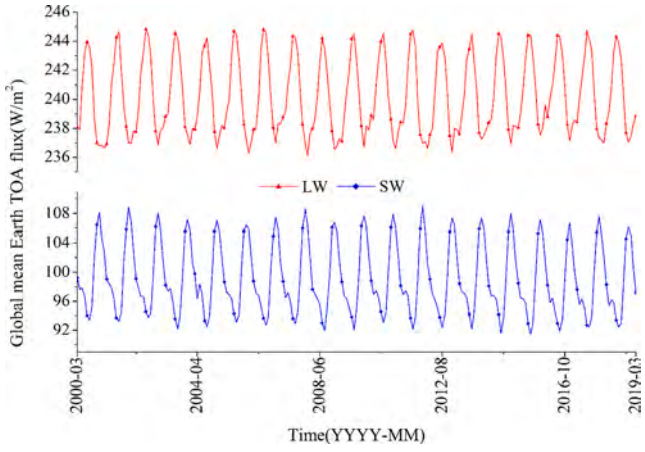

Fig. 12. Monthly means of globally-averaged TOA SW and LW fluxes from March 2000 to March 2019 (data source: CERES Energy Balanced and Filled (EBAF) edition 4.1).

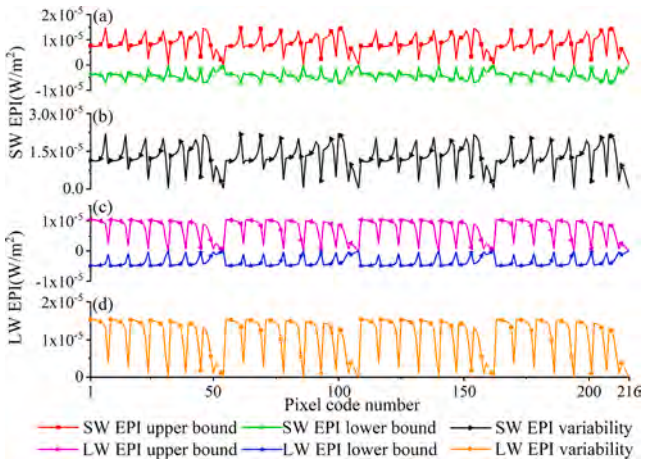

Fig. 13. EPI variation induced by the temporal change of Earth TOA flux for every pixel. (a) the SW EPI upper and lower bounds relative to the monthly mean SW EPI of March 2019 of MERO located at (0°, 0°) (selenographic coordinates), (b) the SW EPI variability (upper bound minus lower bound), (c) the LW EPI upper and lower bounds relative to the monthly mean LW EPI of March 2019 of MERO located at (0°, 0°) and (d) the LW EPI variability (upper bound minus lower bound).

future 18.6-year assessment period (March 2019 to November 2037) were finally derived (Fig. 13) by integrating the EPI sensitivity and Earth TOA flux variation prediction described above. For a pixel, the upper and lower bounds denote the relative maximum and minimum EPIs over the 18.6-year assessment period; the relative maximum and minimum EPIs are derived by subtracting the overall basis (monthly mean EPI of March 2019) from the absolute maximum and minimum EPIs respectively. For example, as shown in Fig. 13 (a), SW EPI of the pixel 1 would vary from -3.72×10^{-6} to 7.62×10^{-6} W/m^2 relative to the overall SW basis of pixel 1 (the monthly mean SW EPI of March 2019 of (0°, 0°) located MERO of pixel 1, that is, 6.98×10^{-5} W/m^2); while the LW EPI of the pixel 1 would fluctuate from -4.94×10^{-6} to 1.04×10^{-5} W/m^2 relative to the overall LW basis of pixel 1 (the monthly mean LW EPI of March 2019 of (0°, 0°) located MERO of pixel 1, that is, 4.51×10^{-4} W/m^2). The Fig. 13 (b) shows that the SW variability is totally consistent with the SW EPI-TOA-flux sensitivity shown in Fig. 11 (a); the same consistency also exists between the LW variability in Fig. 13 (d) and the LW sensitivity in Fig. 11 (b). This is due to the globally mean TOA flux temporal variability used in this study, that is, the TOA flux temporal variabilities for each pixel are the same, which leads to the dominance of EPI-TOA-flux sensitivity over the EPI variability. We here used the globally averaged TOA due to its stability over 20-year period, which rationalize the conservative assumption (the future 19-years interannual change in TOA flux change stays the same as that of the past 19 years). However, this assumption takes no account of the regional difference in the TOA flux temporally change, which may bring certain uncertainty to the evaluation. The regional-scale TOA flux temporal change prediction depends on amounts of factors, such as the cloud and surface type change, the synoptic and regional climate change as well as the anthropogenic activity. We will conduct a systematic study in terms of such a prediction in the future.

4.3. Influence from the MERO's selenographic location

The MERO-Earth geometry depends on the MERO location on the Moon. Therefore, the MERO location would have certain consequences for EPI variability. In this study, we choose 4 selenographic location pairs to reveal such effects: 1. (0°, 0°) and (0°, 81.5° S); 2. (0°, 0°) and (0°, 81.5° N); 3. (0°, 0°) and (80.5° E, 0°); 4. (0°, 0°) and (80.5° W, 0°). These pairs could represent the largest location difference on the Moon based on the MERO deployable region proposed in our previous study

(selegographic latitudinal range: 81.5° S–81.5° N; selegographic longitudinal range: 80.5° W–80.5° E)(Duan et al. 2018). To eliminate the influence from the MERO-Earth geometry temporally change, we utilized the GCC proposed in section 4.2.1 in this evaluation. To erase the effects of anisotropic factor temporal variation, we set the TOA anisotropic-factor-dominant factors (such as the optical depth, the cloud fraction) to be temporally invariant as the monthly mean of March 2019. To eliminate the influence from the Earth TOA flux temporal change, we set the Earth TOA flux temporally invariant as the monthly mean TOA SW and LW fluxes of March 2019. In this assessment, the influence from the MERO location is assessed by the EPI difference between the two same MERO sensors located at two different locations respectively. In particular, this EPI difference is derived by using the EPI of MERO located at (0°, 0°) as the minuend, that is, the location of (0°, 0°) is utilized as the benchmark in this evaluation. The final influence from the MERO location for each pixel is derived through 2 steps: 1. for a pixel, there are 4 EPI difference time series data (March 2019 to November 2037) form 4 location pair respectively; for each EPI difference time series, we separate it to the positive time series and negative time series, then we derive the temporal average values of the positive time series and negative time series; 2. afterwards, for a pixel, there are 4 positive averaged EPI difference and 4 negative average EPI difference from 4 location pairs, respectively; then, we set the maximum of these 4 positive EPI difference as the upper bound and the minimum of these 4 negative averaged EPI difference as the lower bound, finally, we replace the base in this assessment of 18.6-year average EPI of MERO located at (0°, 0°) with the overall basis (monthly mean EPI of March 2019 of MERO located at (0°, 0°)), and adjust the upper and lower bounds. We consider that this upper bound and the lower bound together with the EPI of the MERO located at the origin of the selenographic coordinate system-(0°, 0°), could effectively represent the maximum extent of the influence from the MERO location on the EPI variability. Besides, this combination could provide a interface to integrate this MERO location effect assessment with the above TOA flux and MERO-Earth geometry temporal variation influence evaluations, since these two assessments also uses the overall basis as the benchmark. Final results of EPI variability induced by MERO location change is shown in Fig. 14. For pixel 1, the SW EPI would range from -1.29×10^{-6} to 1.33×10^{-6} W/m^2 relative to the overall SW basis of pixel 1 (the monthly mean SW EPI of March 2019 of (0°, 0°) located MERO of pixel 1, that is, 6.98×10^{-5} W/m^2); the LW EPI would vary from -1.42×10^{-6} to 1.33×10^{-6} W/m^2 relative to the overall LW basis of pixel 1 (the monthly mean LW EPI of March 2019 of (0°, 0°) located MERO of pixel 1, that is, 4.51×10^{-4} W/m^2)(see Fig. 9 (c) and Fig. 10 (c) for the overall SW and LW EPI basis respectively). Fig. 14 (b) and (d) indicate that either the largest SW or LW EPI variability would occurs at the border pixels, such as 8, 16 (see Fig. 2 (b) for the correspondence between pixel location on the FPA and the pixel code number). We think the most plausible reason for this to be that border pixels of two differently located MERO sensors have the largest difference in the pixel-Earth geometry, which would lead to the biggest EPI difference (variation).

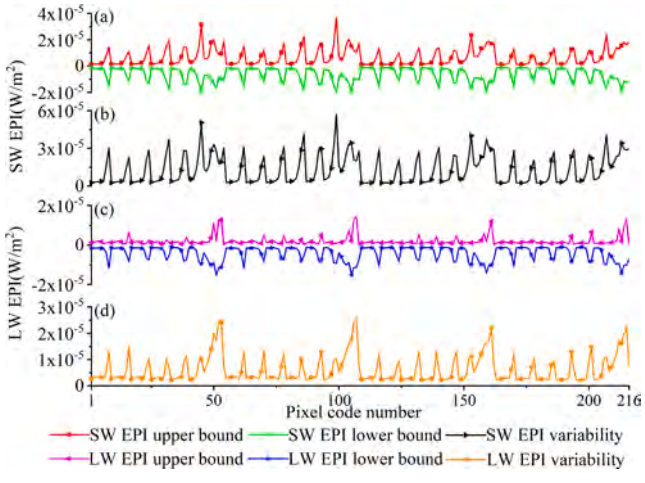

Fig. 14. EPI variation induced by MERO location change for every pixel. (a) The SW EPI upper and lower bounds relative to the monthly mean SW EPI of March 2019 of MERO located at (0°, 0°) (selenographic coordinates), (b) the SW EPI variability (upper bound minus lower bound), (c) the LW EPI upper and lower bounds relative to the monthly mean LW EPI of March 2019 of MERO located at (0°, 0°) and (d) the LW EPI variability (upper bound minus lower bound).

4.4. *Final predictions by integration of the major influences*

The total variability of the SW and LW EPIs for every pixel over the 18.6-year assessment period (March 2019 to November 2037) were finally obtained (Fig. 15), by the overall basis (monthly mean EPI of March 2019) plus the integration of influences from the temporal changes of MERO-Earth geometry, anisotropic factor, and the Earth TOA flux respectively and the effect of MERO location. It was found that the pixel-scale SW EPI would generally range from 3.32×10^{-6} W/m^2 (the least value among all the pixels' absolute minimum SW EPIs) to 2.16×10^{-4} W/m^2 (the highest value among all the pixels' absolute maximum SW EPIs) (Fig. 15 (a)); such a range for the pixel-scale LW EPI is from 4.43×10^{-6} W/m^2 to 4.91×10^{-4} W/m^2 (Fig. 15 (c)). This simulated SW/LW EPI range (i.e., the "realistic incident flux variability) is the core technique requirements of a MERO detector unit. The optimal choice could be reliably made among various detector options by testing their signal qualities and operating stabilities in response to the SW/LW EPI variability derived in this study. Besides, this EPI variability could also be used to judge the afterwards certain systematic parameter adjustment for a MERO system. Furthermore, this "realistic" EPI plays a vital role in defining the detailed specification of the internal calibration module (ICM) of the MERO system (ICM is dedicated to provide the "true" EPI to correct the radiometric calibration function). Fig. 15 (b) shows that the largest SW EPI variability emerge at the high pixels, such as the pixels 7, 15; while the biggest LW EPI variability occurs at the middle pixels, such as pixels 4, 12 (Fig. 15 (d)). This indicate that these pixels would experience larger range of input radiation signal, which may speed up the degradation of the detector units. Therefore, an effective on-orbit calibration procedure especially towards these pixels is necessary to ensure the data quality.

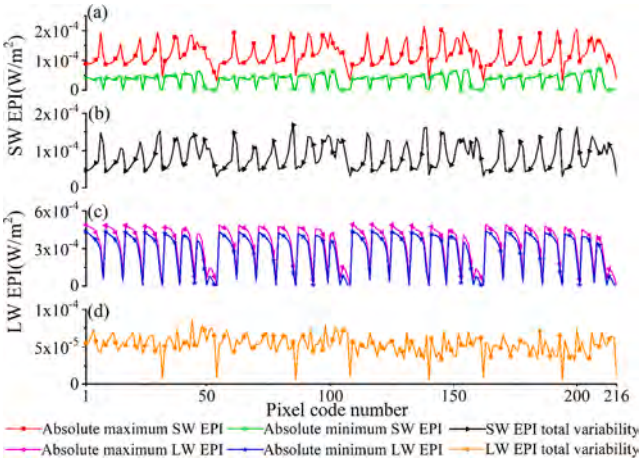

Fig. 15. Total prediction of the pixel-scale EPI variation over the 18.6-year period from March 2019 to November 2037 for every pixel. (a) Absolute maximum and minimum of SW EPI, (b) SW EPI total variability (absolute maximum minus absolute minimum), (c) absolute maximum and minimum of LW EPI and (d) LW EPI total variability (absolute maximum minus absolute minimum).

5. Discussion

In this study, we made an 18.6-year pixel-scale EPI prediction for a MERO system based on the modified pixel-scale EPI quantification methodology. Though a similar EPI prediction has been done in our firstly published EPI work (Duan et al. 2019) (hereafter we abbreviate it as FP1), the prediction research of this study indeed made vital improvements and has larger scientific contribution compared to FP1 (our secondly published study (Duan and Jin 2019) didn't make such a prediction since its EPI quantification methodology possesses key drawbacks, which has been illustrated detailly above in section 3). Scientifically, the EPI prediction in FP1 is made for an unsatisfactory single-pixel MERO sensor, which has little reference value to the applicable multi-pixel MERO sensor. Besides, the TOA radiant anisotropy method used in FP1 is remarkably inaccurate compared to that utilized in this study. Specifically, the FP1 didn't consider the directional anisotropy in the TOA SW outgoing radiance and the TOA LW anisotropy method used in FP1 could bring about 12.15% uncertainty to the derived EPI value (see Fig. 8 (d), notably, our firstly and secondly published EPI studies used the same TOA LW anisotropy method); this makes the prediction results of FP1 less reliable. Conclusively, the EPI prediction in FP1 has less scientific contribution to the MERO sensor design compared to the 18.6-year pixel-scale EPI prediction made in this study. Methodologically, this study brought two vital improvements compared to FP1. This work take account into the effects of the temporal variability of anisotropic factor, which is neglected in FP1. Besides, this study utilized a new parameter-GCC to eliminate the influence from MERO-Earth geometry temporal variability in the assessment of effect of Earth TOA flux temporal change on the pixel-scale EPI variability, while such a case was not considered in FP1.

In this study, we proposed a modified pixel-scale EPI quantification methodology. Such a method could also be used for EPI computation of a satellite-based instrument. However, we warn that such utilization needs certain adjustments, since there is evident difference between the EPI quantification methodology for MERO and that for a man-made satellite. The main discrepancy exists in the pixel-GFOV positioning method, which determines the GFOV position and sensor-Earth geometry. For a MERO system, construction of the pixel-GFOV positioning method is subject to the Moon's orbit characteristics, while construction of that for a man-made satellite would depend on the man-made satellite features. For example, the transform from the MERO FPL (focal plane local coordinate system) to the ECEF coordinate system should consider the temporal variation of lunar libration and the time-dependent inclination and precession of the Moon's orbit; while for a man-made satellite, the sensor-local system transformation mainly considers the satellite position, which depend on the natural factors that drive the satellite orbit change (e.g., gravity) and anthropogenic force (e.g., orbit maintaining maneuver).

When estimating the MERO pixel-scale EPI in this study, we proposed more accurate TOA SW and LW anisotropy methods. However, we argue that some improvements still could be made to these methods. As human population increased enormously in recent decades, the human activities place larger influences to the TOA radiant-anisotropy-dominant factors within the city zone, such as the surface type, the optical depth and the vertical temperature change. This would complicate the TOA radiant anisotropy over the city region. However, the TOA radiant anisotropy method of this study didn't consider this effect.

6. Conclusions

A MERO could advance current ERB study by providing data with less non-simultaneous-sampling uncertainty, higher temporal solution and better polar-region spatial–temporal coverage. The pixel-scale entrance pupil irradiance (EPI), which is the true incident flux to the detector unit of the MERO system, not only plays an important role in the pre-launch instrument design, but also be of importance to the after-launch on-orbit calibration. In this study, we proposed a modified methodology to improve the pixel-scale EPI quantification quality for a MERO sensor. Assessments indicated that the accuracy improvements brought by the new pixel GFOV positioning method are 7.79% and 3.84% for pixel-scale shortwave (SW) EPI and longwave (LW) EPI quantifications respectively; while the newly proposed Earth TOA radiant anisotropy method in this study could lead to accuracy enhancements of 20.67%, and 12.15% for the pixel-scale SW EPI and LW EPI estimations respectively. Based on this modified methodology, an 18.6-year pixel-scale EPI variability prediction was accomplished to facilitate the MERO instrument design coping with change in future decades. This prediction fully considers the influences from the MERO-Earth geometry evolution, anisotropic factor temporal change, the Earth TOA flux temporal variation and MERO location change. Results show that the pixel-scale SW EPI would vary from approximately 3.32×10^{-6} to 2.16×10^{-4} W/m^2 over the future 18.6-year period (March 2019 to November 2037); while the pixel-scale LW EPI would change between 4.43×10^{-6} and 4.91×10^{-4} W/m^2. This EPI variability could act as a referee to optimize the choice among various detector options by testing their signal qualities and operating stabilities in response to the SW/LW EPI variability derived in this study. The EPI variability derived in this work could also be used to judge the afterwards certain systematic parameter adjustment for a MERO system. Furthermore, this EPI range plays a vital role in defining the detailed specification of the internal calibration module (ICM) of the MERO system (ICM is dedicated to provide the "true" EPI to correct the radiometric calibration function).

Declaration of Competing Interest

The authors declare that they have no known competing financial interests or personal relationships that could have appeared to influence the work reported in this paper.

Acknowledgments

This work was supported by the Strategic Priority Research Program Project of the Chinese Academy of Sciences (Grant No. XDA23040100), Startup Foundation for Introducing Talent of NUIST under Grant 2019r086, and Experiments for Space Exploration Program of the Qian Xuesen Laboratory, China Academy of Space Technology (Grant No. TKTSPY-2020-06-02).

References

Barkstrom, B., Harrison, E., Smith, G., Green, R., Kibler, J., Cess, R., the ERBE Science Team, 1989. Earth radiation budget experiment (ERBE) archival and April 1985 results. Bull. Am. Meteorol. Soc. 70 (10), 1254–1262.

Brown, P.T., Caldeira, K., 2017. Greater future global warming inferred from Earth's recent energy budget. Nature 552 (7683), 45–50.

Czapla-Myers, J., McCorkel, J., Anderson, N., Thome, K., Biggar, S., Helder, D., Aaron, D., Leigh, L., Mishra, N., 2015. The Ground-Based Absolute Radiometric Calibration of Landsat 8 OLI. Remote Sens. 7 (1), 600–626.

Dewitte, S., Gonzalez, L., Clerbaux, N., Ipe, A., Bertrand, C., & De Paepe, B., 2008. The Geostationary Earth Radiation Budget Edition 1 data processing algorithms. Adv. Space Res., 41, 1906–1913.

Duan, W., Huang, S., Nie, C., 2018. Conceptual design of a Moon-based Earth radiation observatory. Int. J. Remote Sens. 39 (18), 5834–5849.

Duan, W., Huang, S., Nie, C., 2019. Entrance Pupil Irradiance Estimating Model for a Moon-Based Earth Radiation Observatory Instrument. Remote Sens. 11 (5), 583. https://doi.org/10.3390/rs11050583.

Duan, W., & Jin, S., 2019. A Model of Entrance Pupil Irradiance Estimation of the Multi-pixel Sensor on a Moon-based Earth Radiation Observatory. In: 2019 Photonics & Electromagnetics Research Symposium - Fall (PIERS - Fall), pp. 1966–1970.

Forster, P.M.F., Gregory, J.M., 2006. The Climate Sensitivity and Its Components Diagnosed from Earth Radiation Budget Data. J. Clim. 19, 39–52.

Guo, H., Dou, C., Zhang, X., Han, C., Yue, X., 2016. Earth observation from the manned low Earth orbit platforms. ISPRS J. Photogramm. Remote Sens. 115, 103–118.

Guo, H., Fu, W., Liu, G. (Eds.), 2019. Scientific Satellite and Moon-Based Earth Observation for Global Change. Springer Singapore, Singapore.

Hall, J.V., Zhang, R., Schroeder, W., Huang, C., Giglio, L., 2019. Validation of GOES-16 ABI and MSG SEVIRI active fire products. Int. J. Appl. Earth Obs. Geoinf. 83, 101928. https://doi.org/10.1016/j.jag.2019.101928.

Haran, T.L., James, J.C., Lane, S.E., Cincotta, T.E., 2019. Quantum efficiency and spatial noise tradeoffs for III–V focal plane arrays. Infrared Phys. Technol. 97, 309–318.
Harries, J.E., Russell, J.E., Hanafin, J.A., Brindley, H., Futyan, J., Rufus, J., Kellock, S., Matthews, G., Wrigley, R., Last, A., Mueller, J., Mossavati, R., Ashmall, J., Sawyer, E., Parker, D., Caldwell, M., Allan, P.M., Smith, A., Bates, M.J., Coan, B., Stewart, B.C., Lepine, D.R., Cornwall, L.A., Corney, D.R., Ricketts, M.J., Drummond, D., Smart, D., Cutler, R., Dewitte, S., Clerbaux, N., Gonzalez, L., Ipe, A., Bertrand, C., Joukoff, A., Crommelynck, D., Nelms, N., Llewellyn-Jones, D.T., Butcher, G., Smith, G.L., Szewczyk, Z.P., Mlynczak, P.E., Slingo, A., Allan, R.P., Ringer, M.A., 2005. The geostationary earth radiation budget project. Bull. Am. Meteorol. Soc. 86 (7), 945–960.
Kopp, G., Lean, J.L., 2011. A new, lower value of total solar irradiance: Evidence and climate significance. Geophys. Res. Lett. 38 (1), n/a–n/a.
Loeb, N.G., 2017. CERES SYN ED4A DATA quality. NASA Atmospheric Science Data Center (ASDC), Hampton, VA, USA.
Loeb, N.G., Kato, S., Loukachine, K., Manalo-Smith, N., 2005. Angular Distribution Models for Top-of-Atmosphere Radiative Flux Estimation from the Clouds and the Earth's Radiant Energy System Instrument on the Terra Satellite. Part I: Methodology. J. Atmos. Oceanic Technol. 22, 338–351.
Loeb, N.G., Kato, S., Loukachine, K., Manalosmith, N., 2003. Angular Distribution Models for Top-of-Atmosphere Radiative Flux Estimation from the Clouds and the Earth's Radiant Energy System Instrument on the Terra Satellite. Part I: Methodology. J. Appl. Meteorol. 42, 240–265.
Luther, M.R., Cooper, J.E., Taylor, G.R., 1986. The Earth Radiation Budget Experiment Nonscanner Instrument. Rev. Geophys. 24 (2), 391. https://doi.org/10.1029/RG024i002p00391.
Marshak, A., Herman, J., Adam, S., Karin, B., Carn, S., Cede, A., Geogdzhayev, I., Huang, D., Huang, L.-K., Knyazikhin, Y., Kowalewski, M., Krotkov, N., Lyapustin, A., McPeters, R., Meyer, K.G., Torres, O., Yang, Y., 2018. Earth Observations from DSCOVR EPIC Instrument. Bull. Am. Meteorol. Soc. 99, 1829–1850.
Nagol, J.R., Sexton, J.O., Kim, D.-H., Anand, A., Morton, D., Vermote, E., Townshend, J. R., 2015. Bidirectional effects in Landsat reflectance estimates: Is there a problem to solve? ISPRS J. Photogramm. Remote Sens. 103, 129–135.
Rogalski, A., 2010. Infrared detectors. CRC Press, New York, NY, USA, pp. 645–676.
Rogalski, A., 2012. Progress in focal plane array technologies. Prog. Quantum Electron. 36 (2-3), 342–473.
Smith, G.L., Priestley, K.J., Loeb, N.G., 2014. Clouds and Earth Radiant Energy System: From Design to Data. IEEE Trans. Geosci. Remote Sens. 52 (3), 1729–1738.
Smith, G.L., Wong, T., Bush, K.A., 2015. Time-Sampling Errors of Earth Radiation From Satellites: Theory for Outgoing Longwave Radiation. IEEE Trans. Geosci. Remote Sens. 53 (3), 1656–1665.
Su, W., Corbett, J., Eitzen, Z., Liang, L., 2015. Next-generation angular distribution models for top-of-atmosphere radiative flux calculation from CERES instruments: methodology. Atmos. Meas. Tech. 8 (2), 611–632.
Su, W., Minnis, P., Liang, L., Duda, D.P., Khlopenkov, K., Thieman, M.M., Yu, Y., Smith, A., Lorentz, S., Feldman, D., Valero, F.P.J., 2020. Determining the daytime Earth radiative flux from National Institute of Standards and Technology Advanced Radiometer (NISTAR) measurements. Atmos. Meas. Tech. 13 (2), 429–443.
Thorne, K., Markharn, B., Barker, P.S., Biggar, S., 1997. Radiometric calibration of Landsat. Photogramm. Eng. Remote Sens. 63, 853–858.
Trenberth, K.E., Fasullo, J.T., Kiehl, J., 2009. Earth's global energy budget. Bull. Am. Meteorol. Soc. 90 (3), 311–324.
Trepte, Q.Z., Minnis, P., Sun-Mack, S., Yost, C.R., Chen, Y., Jin, Z., Hong, G., Chang, F., Smith, W.L., Bedka, K.M., Chee, T.L., 2019. Global Cloud Detection for CERES Edition 4 Using Terra and Aqua MODIS Data. IEEE Trans. Geosci. Remote Sens., 57, 9410–9449.
Wielicki, B.A., Wong, T., Allan, R.P., Slingo, A., Kiehl, J.T., Soden, B.J., Gordon, C.T., Miller, A.J., Yang, S.-K., Randall, D.A., Robertson, F., Susskind, J., Jacobowitz, H., 2002. Evidence for large decadal variability in the tropical mean radiative energy budget. Science 295 (5556), 841–844.
Wong, T., Smith, G.L., Kato, S., Loeb, N.G., Kopp, G., Shrestha, A.K., 2018. On the Lessons Learned From the Operations of the ERBE Nonscanner Instrument in Space and the Production of the Nonscanner TOA Radiation Budget Data Set. IEEE Trans. Geosci. Remote Sens. 56 (10), 5936–5947.
Zhou, C., Zelinka, M.D., Klein, S.A., 2016. Impact of decadal cloud variations on the Earth's energy budget. Nat. Geosci. 9 (12), 871–874.